AIAA JOURNAL
Vol. 40, No. 7, July 2002

Velocity Measurements in a Pressure-Driven Three-Dimensional Compressible Turbulent Boundary Layer

Brad A. Boswell*
Sandia National Laboratories, Albuquerque, New Mexico 87185
and
J. Craig Dutton†
University of Illinois at Urbana–Champaign, Urbana, Illinois 61801

The flow characteristics of a three-dimensional, compressible, turbulent boundary layer have been investigated experimentally. The three dimensionality was generated by inclining a cylindrical afterbody at 10-deg angle of attack to a Mach 2.45 freestream. The objective was to determine the mechanisms that govern the growth and behavior of pressure-driven, three-dimensional, compressible, turbulent boundary layers. Laser Doppler velocimetry was used to determine mean velocity components and turbulence statistics. The results show a significantly thicker boundary layer on the leeward side of the body than in the windward region. This circumferential variation in boundary-layer thickness is caused by the pressure-driven circumferential flow, which provides a mass surplus in the low-pressure, leeward region and a mass deficit in the high-pressure, windward portion of the boundary layer. In addition, the pressure discontinuity at the angular junction and the axial pressure gradient also play a role in the boundary-layer growth. Turbulent normal and shear stresses peak very near the wall, with an initial streamwise peak forming at the interaction of the oblique shock/expansion fan with the boundary layer. The highly turbulent fluid on the windward side of the body is transported toward the leeward region by the circumferential flow in the boundary layer.

Nomenclature

C_f = skin-friction coefficient
H = compressible shape factor, δ^*/θ
P = static pressure
R = afterbody base radius, 31.75 mm
r = radial coordinate
r^* = radial coordinate of approach flow
u_τ = friction velocity
V = mean velocity
v' = fluctuating velocity
x = axial coordinate
x^* = axial coordinate of approach flow
α = angle of attack
δ = boundary-layer thickness
δ^* = boundary-layer displacement thickness
θ = boundary-layer momentum thickness
Π = boundary-layer wake strength parameter
ρ = fluid density
ϕ = circumferential coordinate

Subscripts

i = incompressible result
r = radial component
x = axial component
x^* = approach axial component
∞ = freestream value

Introduction

THE inclination of rockets, missiles, and other axisymmetric aerodynamic bodies to nonzero angle of attack causes an asymmetrical pressure field about the body, providing a three-dimensional driving force that creates a finite circumferential velocity in the boundary layer. If the aerodynamic body is flying at supersonic velocities while inclined at angle of attack, the three-dimensional pressure gradient about the boundary layer is further complicated by the presence of a pressure discontinuity, that is, oblique shock or expansion fan, of circumferentially varying strength at the onset of the three-dimensional interaction. The behavior of a three-dimensional boundary layer of this type affects design parameters such as skin-friction drag on the body and also plays a critical role in flow structural features such as leeside separation vortices. In turn, these features interact with the separated flow region in the near wake, thereby affecting the base drag and wake structure. Thus, understanding the behavior of these three-dimensional boundary layers is important in improving the design and control of cylindrical supersonic bodies inclined at angle of attack.

The general flow structure about a cylindrical slender body at angle of attack is well understood. Oblique shocks and expansion waves existent at the projectile forebody provide a pressure and velocity discontinuity at the onset of the three-dimensional interaction. Flow is driven from windward to leeward along the body and may result in the formation of leeside vortices (symmetric or asymmetric) depending on the combination of angle of attack, body length, and freestream velocity.[1] However, the detailed characteristics and behavior of the pressure-driven, three-dimensional boundary layer at the surface of the body are not well understood.

Significant effort has been expended in the measurement of velocities in three-dimensional incompressible boundary layers. Experimental studies of three-dimensional boundary layers have been conducted for low speeds in a variety of geometries with the three dimensionality created by both pressure gradients and surface shear stresses.[2] In one particularly relevant study, Chesnakas and Simpson[3] measured all three velocity components and the complete turbulent stress tensor in the boundary layer near the separation point on the leeward surface of a prolate spheroid. This geometry closely resembles the flow over the forebody of an axisymmetric projectile in subsonic flight.

The available experimental velocity data for three-dimensional boundary layers with supersonic freestream velocities are quite limited. Several researchers have studied the three-dimensional

Received 28 July 2001; revision received 4 March 2002; accepted for publication 5 March 2002.

*Senior Member of Technical Staff, Department 2114. Member AIAA.
†W. Grafton and Lillian B. Wilkins Professor, Department of Mechanical and Industrial Engineering. Associate Fellow AIAA.

boundary layers generated downstream of oblique shocks created at both inclined and swept fins on flat surfaces.[4–6] Another experiment used a fin designed with increasing curvature to study the effects of gradual increases in three dimensionality on both the mean velocity and turbulence behavior of a boundary layer in supersonic flow.[7–9] In particular, the study in Ref. 8 showed that in-plane streamline curvature tends to stabilize turbulence intensities. Although these studies provide valuable insight into the development of three-dimensional, pressure-driven boundary layers, each involves boundary-layer growth over a flat surface, which does not entail the surface curvature effects of a body of revolution at angle of attack. To account for these surface curvature effects, researchers have measured velocities in three-dimensional boundary layers generated from two-dimensional, axisymmetric boundary layers by adding an offset flare junction to the flow along a cylinder.[10] In addition, velocity measurements have been made in the boundary layer around cones inclined at angle of attack to generate three dimensionality.[11–14] Although these studies do not precisely match the geometry of the cylindrical main body of an aerodynamic projectile, they do provide a similar circumferential pressure gradient to that imposed on an axisymmetric body in nonzero-angle-of-attack supersonic flight.

In the current investigation, experiments were conducted to measure the velocity field in the three-dimensional boundary layer about a cylindrical afterbody aligned at angle of attack in a supersonic freestream. Laser Doppler velocimetry (LDV) measurements were made at numerous spatial locations about the afterbody to provide the mean velocity field and turbulence statistics in the boundary layer along three meridional planes. The measurements were located in both the windward and leeward planes and also in a side plane at the circumferential midpoint between the windward and leeward regions. The velocity data are compared to previously obtained surface streakline patterns and surface pressure data in the same flow[15] to determine the effect of three dimensionality on the boundary-layer development. These measurements help to improve understanding of three-dimensional, compressible, turbulent boundary-layer development under pressure-driven conditions and provide an experimental database for the validation and improvement of numerical models of three-dimensional, compressible boundary layers. In addition, the data provide an initial condition for use in the numerical modeling of supersonic base flows at angle of attack.

Experimental Facilities and Procedures

A blowdown-type wind tunnel designed specifically for the study of axisymmetric base flows was used to complete these experiments. The facility has previously been used to make velocity measurements in the base region of supersonic axisymmetric base flows with and without base bleed.[16,17] In this facility, dried and compressed air passes from a stagnation chamber, through a flow conditioning section, and into an annular converging–diverging (C–D) nozzle. For the current experimental conditions, with a stagnation pressure of 565 kPa and stagnation temperature of 300 K, the C–D nozzle provides an axisymmetric flow with a nominal freestream Mach number of 2.5 as the flow passes into the test section. The airflow exits the facility through a diffuser and silencing duct. Windows in the test section provide optical access to the afterbody surface from three sides to allow for nonintrusive laser-diagnostic measurements.

The experimental afterbody is supported by an annular sting running along the tunnel centerline, which is supported far upstream of the C–D nozzle to prevent support interference effects from entering the measurement region. A schematic of the experimental afterbody and the flowfield studied here is included in Fig. 1. The cylindrical afterbody has a length-to-radius ratio of 3.0 and is inclined at a 10-deg angle of attack relative to the freestream flow. Figure 2 shows a previously reported oil-streak visualization of the surface flow generated on this afterbody.[15] Clearly, the 10-deg angle of attack provides sufficient three dimensionality to transport fluid from the windward to leeward portions of the afterbody. A cylindrical coordinate system (Fig. 1) is used throughout this study aligned along the axis of the afterbody with positive axial x values oriented in the downstream direction. Radial distance r is measured from the axis, and circumferential angle ϕ is measured from 0 deg on the windward surface to 180 deg on the leeward surface of the afterbody in a clockwise direction as observed from upstream. For measurement of the approach boundary layers, the coordinate system is rotated so that the radial coordinate r^* is measured from the sting centerline and normal to the freestream approach direction. Axial distance x^* is measured parallel to the freestream approach direction, and circumferential angle is measured as discussed earlier.

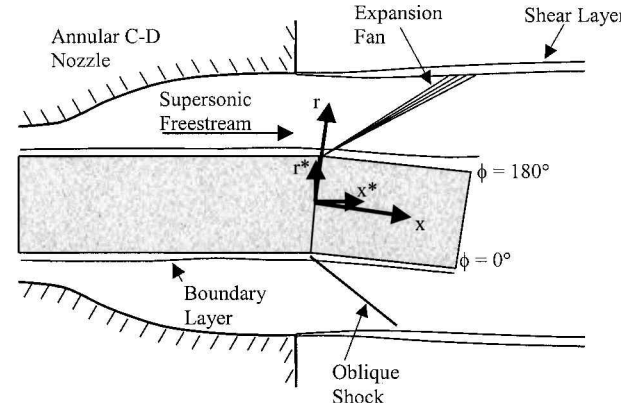

Fig. 1 Schematic of angle-of-attack afterbody and coordinate systems.

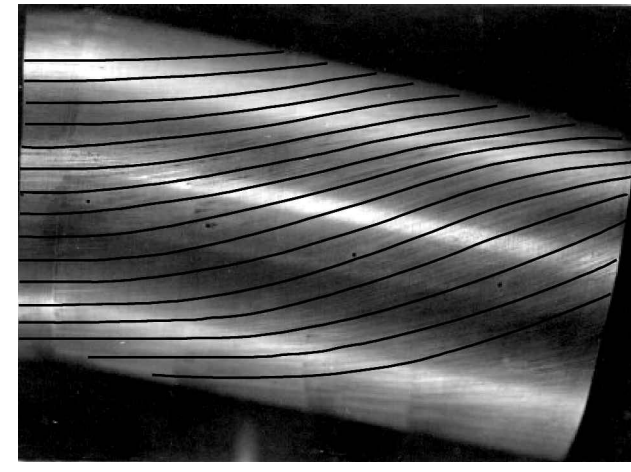

Fig. 2 Oil-streak visualization of $\phi = -90$ deg surface (from Ref. 15).

A two-component dual-beam LDV system was used in these experiments with a 7-W argon-ion laser generating green (514.5-nm) and blue (488-nm) beams. The probe volume formed by this four-beam crossing is 165 μm in diameter. The fringe spacing of each beam pair is 14.5 and 13.6 μm for the green and blue beams, respectively. The beam pairs are rotated to approximately ± 45 deg from the incoming freestream direction to reduce fringe blindness. Bragg cells provide a 40-MHz frequency shift to reduce fringe biasing and discriminate reverse velocities. The intensity of light scattered from seed particles was collected at a 20-deg off-axis forward-scatter location and is converted to an analog voltage signal by two photomultiplier tubes. The off-axis collection location and pinhole aperture in the receiving optics provide an effective probe volume length of 730 μm. A TSI IFA-750 autocorrelation processor was used to convert the photomultiplier tube voltage signal into the corresponding velocity. Data were collected using an Intel Celeron-based personal computer for processing and analysis. Control of the LDV probe volume location was maintained through use of a three-axis, computer-controlled traverse system with a spatial resolution of ± 1.5 μm in all directions.

Seeding for the LDV measurements was provided by a six-jet atomizer that supplied silicone oil droplets to the flow through three tubes located downstream of the flow conditioning section and separated by 120 deg circumferentially. The seeding system produces droplets with a mean diameter of approximately 0.8 μm, which Bloomberg[18] has shown to be sufficiently small that any false turbulence created in the flow due to the polydispersion of the silicone

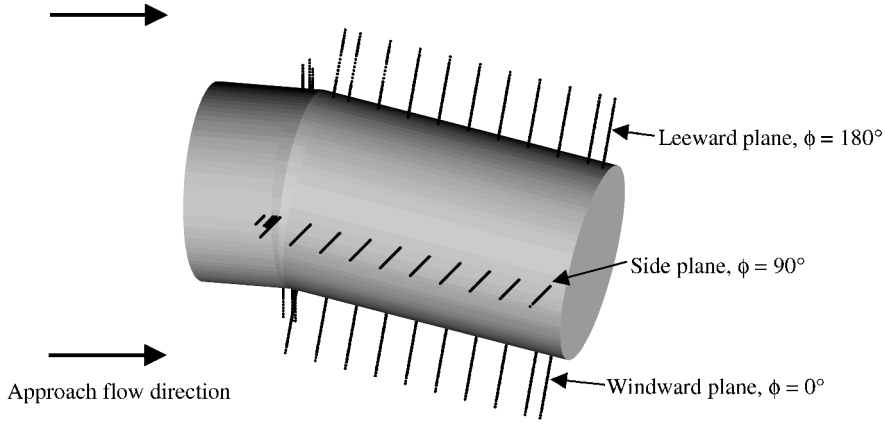

Fig. 3 LDV measurement locations in afterbody boundary layer.

droplet size is small compared to the overall turbulence level. In addition, Bloomberg[18] estimated a 2-mm particle lag region for identical silicone droplets passing through a 15-deg compression corner in a Mach 2.6 flow. Because the freestream Mach number is lower and the turning angle less severe in the current results than in the study of Bloomberg, particle lag effects should be confined to within 2 mm of the discontinuity in the current investigation.

A series of radial profiles was measured using the LDV system, with the measurements concentrated in the boundary layer of the approach flow and in the windward ($\phi = 0$ deg), leeward ($\phi = 180$ deg), and side ($\phi = 90$ deg) planes of the afterbody boundary layer, as seen in Fig. 3. In the approach boundary layer, 9 radial traverses were completed, whereas 10, 10, and 11 profiles were measured in the windward, side, and leeward planes, respectively. In each radial traverse, 40–66 spatial locations were included, with 4000 individual velocity realizations stored at most spatial locations for the computation of mean velocity and turbulence statistics. The effects of velocity bias on the LDV data were corrected using an interarrival time-weighting scheme, which has been shown to be effective as a debiasing tool in compressible shear flows of this type.[19] With this two-component LDV arrangement, both the streamwise and radial components of the mean velocity were measured simultaneously, but no measurements of the circumferential velocity component (which should have a zero mean value for the $\phi = 0$ and 180 deg data planes) were obtained. In addition, both streamwise and radial Reynolds normal stresses, $\langle v_x'^2 \rangle$ and $\langle v_r'^2 \rangle$, and the axial–radial Reynolds shear stress, $-\langle v_x' v_r' \rangle$, have been measured directly. The worst-case uncertainty in mean velocity and rms velocity fluctuations is estimated to be 1.2 and 2.3% of the mean freestream velocity, $V_\infty = 573$ m/s, respectively.[20]

Results and Discussion

Approach Boundary-Layer Velocity Measurements

Upstream of the angular discontinuity, nine individual boundary-layer velocity profiles were measured, with three profiles each measured in the $\phi = 0$-, 90-, and 180-deg circumferential planes at different axial locations. The approach mean velocity profiles shown in Fig. 4 are representative of the incoming velocity field at each angular position. Each velocity profile reveals a fully developed, compressible, turbulent boundary layer with no apparent interference waves impinging on it. The profiles for the various ϕ positions collapse reasonably well, suggesting that the sting is well centered on the tunnel axis. These experimental data were curve fitted to the theoretical profile of Sun and Childs,[21] which was developed for turbulent, compressible boundary layers. Boundary-layer parameters and integral thicknesses were then determined based on the theoretical curve fit to the experimental data. The average of these nondimensional values for the three angular stations measured at $x^*/R = -0.031$ is included in Fig. 4. These nondimensional values are consistent with those previously measured for axisymmetric approach boundary layers in the same facility.[16,22] The measured freestream velocity of 573 m/s corresponds to a Mach number of 2.45, and the resulting unit Reynolds number was calculated as

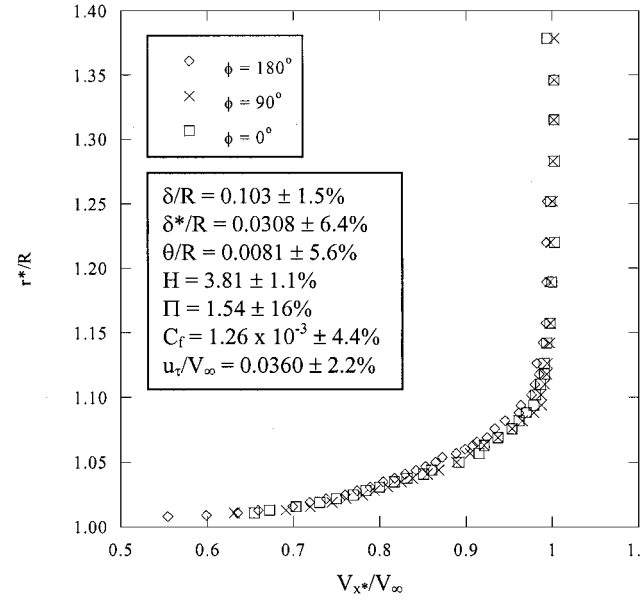

Fig. 4 Average approach flow streamwise velocity profiles and average approach boundary-layer statistics.

56×10^6 m^{-1}. Directly measured streamwise turbulence intensities throughout the approach freestream were consistently less than 2%. The turbulence intensities peak at approximately 8% in the inner portion of the boundary layer.

Mean Velocity and Boundary-Layer Thickness Measurements

Contours of dimensionless velocity magnitude $(V_x^2 + V_r^2)^{1/2}/V_\infty$ in the $\phi = 0$-, 90-, and 180-deg planes are included in Figs. 5a–5c, respectively. Note that, in each case, the radial coordinate has been stretched with respect to the axial coordinate to better observe the boundary-layer interaction. In addition, for each contour plot, the body surface is located at the bottom edge of the plot at $r/R = 1$. (See Fig. 3 for orientation.) To present these contour plots, the LDV data were passed twice through a five-point smoothing filter with a smoothing coefficient of 0.5. In addition to the dimensionless velocity magnitude contours, Fig. 5 shows the two-dimensional flow streamlines in each plane that were generated by integrating the mean (V_x, V_r) velocity data.

The velocity magnitude results in the windward region (Fig. 5a) show the flow deceleration behind the compression shock created at the angular discontinuity $x/R = 0$. Note that the slight apparent waviness in the shock is caused by interpolation between the discretely spaced velocity data. The dashed line in Fig. 5a represents the location of a compression shock created at a 10-deg planar compression corner based on compressible flow theory. The streamlines begin to turn at a location very close to that of the theoretical

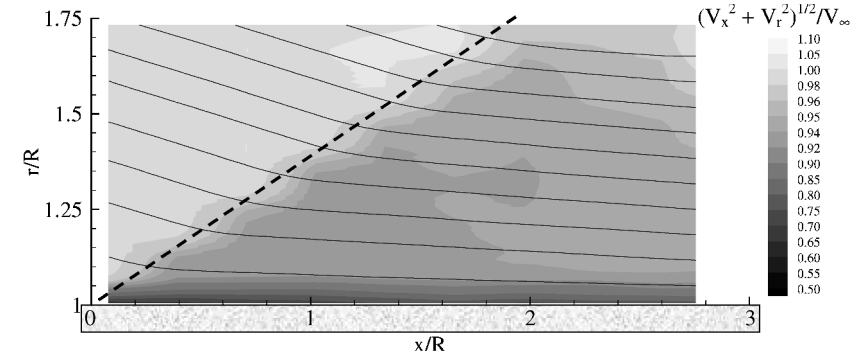

a) Windward plane, $\phi = 0$ deg

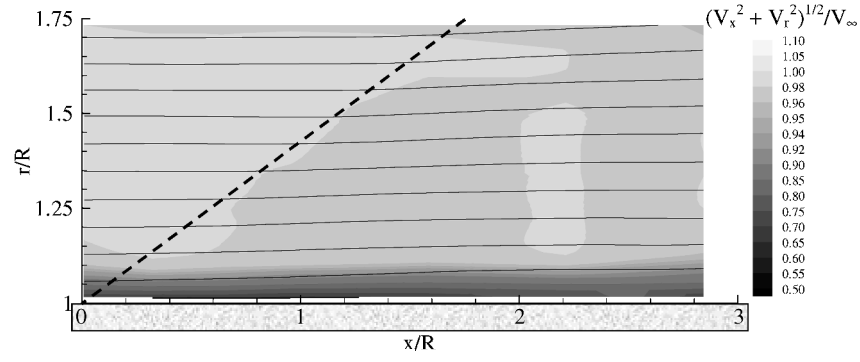

b) Side plane, $\phi = 90$ deg

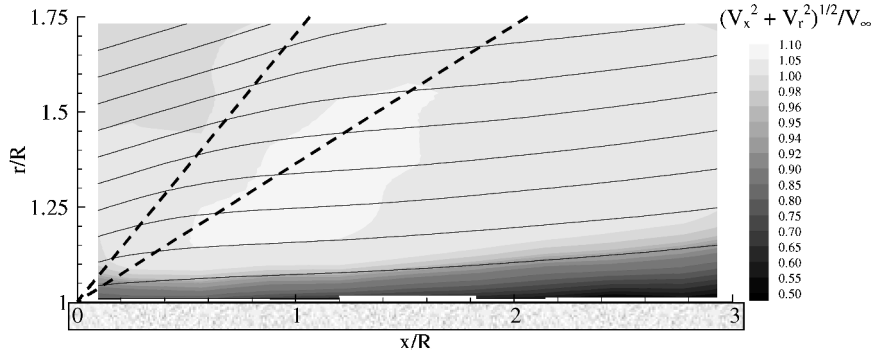

c) Leeward plane, $\phi = 180$ deg

Fig. 5 V_x–V_r velocity magnitude contours and representative streamlines.

planar compression wave. The gradual turning of the flow streamlines across the compression wave results at least partially from particle lag, where a relaxation distance of less than 2 mm is expected for the given freestream flow velocity and compression angle. Behind the shock, the streamlines do not completely turn 10 deg to match the surface orientation, but instead continue to approach the surface. The streamline convergence at the windward surface results from the windward-to-leeward circumferential flow,[15] which creates an efflux of mass from the windward portion of the boundary layer. This circumferential mass efflux also appears to result in a slight thinning of the boundary layer with increased axial position along the afterbody.

The velocity magnitude data on the side plane (Fig. 5b) show a slight flow deceleration behind a weak oblique shock that occurs at the cylinder/afterbody junction. This agrees with the previously obtained surface pressure data,[15] which show a weak compression occurring at the angular discontinuity $x/R = 0$ in the $\phi = 90$ deg plane. Note that the velocity magnitude change in this region is very small (approximately 2.7%), and the streamlines remain almost straight in the region of the weak compression, which suggests that the wave behaves almost as a Mach wave. In fact, the location of the flow deceleration portrayed by the velocity data closely matches the location of a Mach wave in Mach 2.45 flow (the Mach angle is 23.4 deg), as represented by the dashed line in Fig. 5b. The boundary layer appears to remain fairly constant in thickness throughout the measurement region on the side plane, except in the most downstream region (see subsequent discussion). Note that the velocity magnitude results in the side plane (shown in Fig. 5b) do not include the circumferential velocity component, which is clearly nonzero in this measurement region. However, directly downstream of the angular discontinuity, the circumferential velocity component should be very small (because the disturbance to the flow is minimized in this plane) and, thus, should not significantly affect the velocity magnitude gradient at the angular junction. Farther downstream, however, the effect of the circumferential velocity on the transport of fluid about the cylinder may affect the growth and development of the boundary layer in this plane.

The velocity magnitude results in the leeward region (Fig. 5c) reveal a flow acceleration created by an expansion fan centered at the angular discontinuity $x/R = 0$. The dashed lines in Fig. 5c represent the extent of a Prandtl–Meyer expansion fan centered at a 10-deg planar expansion turn based on isentropic compressible flow theory. The streamlines begin to turn at a location approximately corresponding to the location of the theoretical planar expansion fan, although it appears that the flow rotation may begin slightly upstream of that predicted by two-dimensional theory. Downstream of

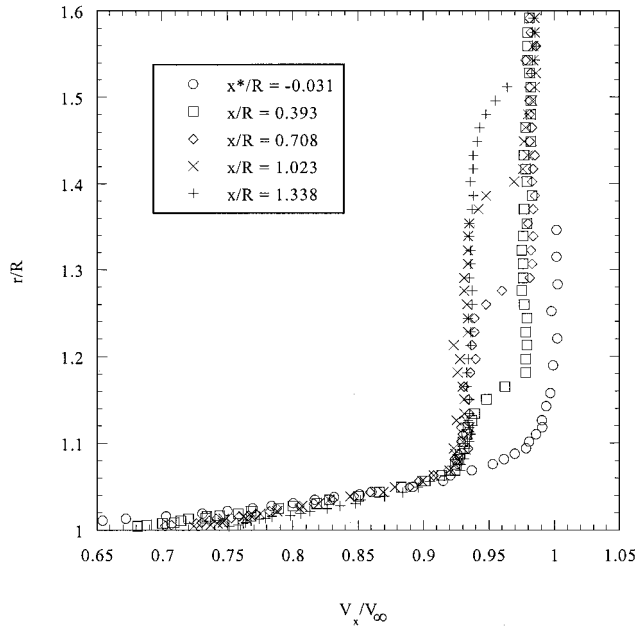

Fig. 6 Axial velocity development near angular discontinuity in windward plane.

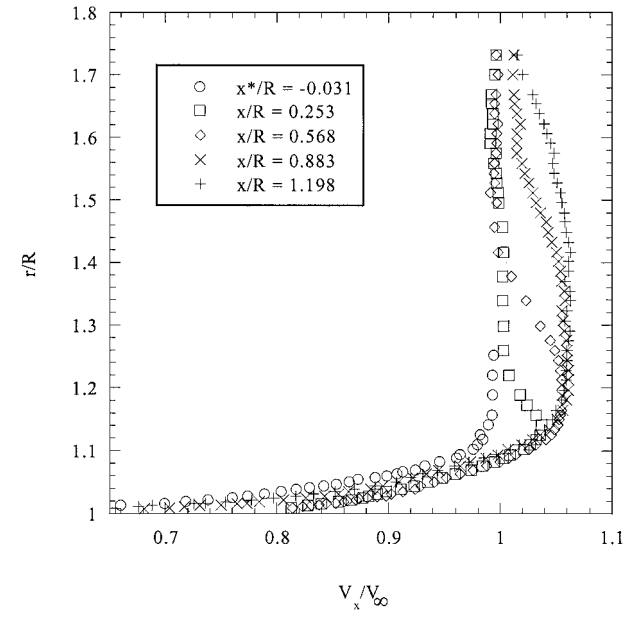

Fig. 7 Axial velocity development near angular discontinuity in leeward plane.

the expansion fan, the streamlines appear to approach straight-line shapes but then begin to curve away from the leeward surface (i.e., there is an inflection in the streamlines downstream of the expansion) in the downstream region of the measurement domain. This curvature is most likely caused by the previously observed windward-to-leeward circumferential flow about the afterbody,[15] which creates an influx of mass to the leeward portion of the boundary layer. This mass entrainment in the leeward portion of the boundary layer would also account for, at least partially, the apparent growth of the boundary layer with axial distance.

Additional insight into the initial spatial development of the boundary layer near the velocity discontinuity may be gained by investigating individual velocity profiles just downstream of the angular junction. The spatial evolution of axial velocity in the windward plane is shown in Fig. 6. Note that, although a velocity profile was measured at $x/R = 0.078$, the presence of the oblique shock within the boundary layer at this location resulted in particle lag effects in the boundary layer, thus preventing the identification of the behavior with confidence. As a result, boundary-layer profiles are not presented directly downstream of the angular discontinuity at locations where the shock is within the boundary layer. The location of the compression shock is clearly evident outside the boundary layer in all profiles for $x/R \geq 0.393$, as seen in Fig. 6. The compression across the oblique shock appears to increase slightly the mean axial velocity in the boundary layer very near the wall, $r/R < 1.02$, whereas the velocity decreases slightly from the approach velocity profile near the edge of the boundary layer, $r/R \approx 1.06$. The downstream velocity profiles appear to maintain a similar shape with increasing x, which suggests a recovery toward an equilibrium state downstream of the shock, as observed in the data of Kuntz et al.[23] for a planar 12-deg compression corner in Mach 2.94 flow. However, for the equilibrium condition reached in the two-dimensional data,[23] the axial velocity downstream of the shock remains significantly lower than the approach velocity at all radial locations.

The corresponding axial velocity development near the angular discontinuity in the leeward plane is included in Fig. 7. The presence of the expansion fan is clearly evident in the downstream profiles as a widening region of acceleration beyond the freestream approach velocity. Close to the wall, the expansion fan appears to accelerate the fluid velocity compared to the approach flow at the first few axial locations, although the velocity profile begins to recover toward the approach conditions with increasing x. This recovery toward the approach velocity conditions in the inner portion of the boundary layer occurs over a much longer axial distance than observed in the windward plane boundary layer, which suggests that flow three dimensionality delays the return to equilibrium conditions in the inner portion of the boundary layer in the leeward plane.

The axial variation in boundary-layer thickness was quantified by integrating the mean velocity profiles to calculate the incompressible boundary-layer displacement thickness:

$$\delta_i^* = \int_R^\infty \left(1 - \frac{V_x}{V_{x,\infty}}\right) \mathrm{d}r \tag{1}$$

Note that compressible displacement thickness is not presented here because there is a possibility of radial pressure variations across this three-dimensional boundary layer, thus preventing the estimation of density variations with confidence. In addition, the freestream velocity at the edge of the boundary layer $V_{x,\infty}$ varies axially in all three planes due to three-dimensional effects outside the boundary layer. Because of the direct interaction of the oblique shock/expansion fan and boundary layer (Figs. 6 and 7), the value of $V_{x,\infty}$ could not be determined with certainty just downstream of the angular discontinuity. As a result, the displacement thickness has not been presented for the first few axial stations downstream of the angular discontinuity. The displacement thickness along the $\phi = 0$, 90, and 180 deg planes is plotted in Fig. 8b, together with previously measured surface pressure data[15] (Fig. 8a) along these same planes.

In the windward region, the boundary layer is compressed to a displacement thickness 0.44 times the approach thickness. The majority of this δ_i^* change appears to occur near the angular junction, where the pressure increase across the compression shock forces a reduction in boundary-layer thickness. After this initial compression, two additional factors prevent the growth of the boundary layer during its axial development in the windward plane. First, a favorable pressure gradient occurs on the windward surface for $x/R > 0.5$, retarding an increase in δ_i^*. Second, the windward-to-leeward circumferential flow about the afterbody (as seen in Fig. 2) provides a mass efflux from the windward region that also prevents boundary-layer growth.

In the side region, $\phi = 90$ deg, the displacement thickness initially remains relatively constant throughout its streamwise development before growing to 1.96 times larger than the approach value toward the end of the measurement domain. Initially, the circumferential mass flux effects in this region should generally be small as windward fluid merely passes through the side plane in its passage toward the leeward region for most of the afterbody length. Thus, the first neutral then favorable pressure gradient is the main factor contributing to boundary-layer development in the side plane. The displacement thickness growth near the end of the afterbody in the side plane may result from the mass surplus that accumulates in

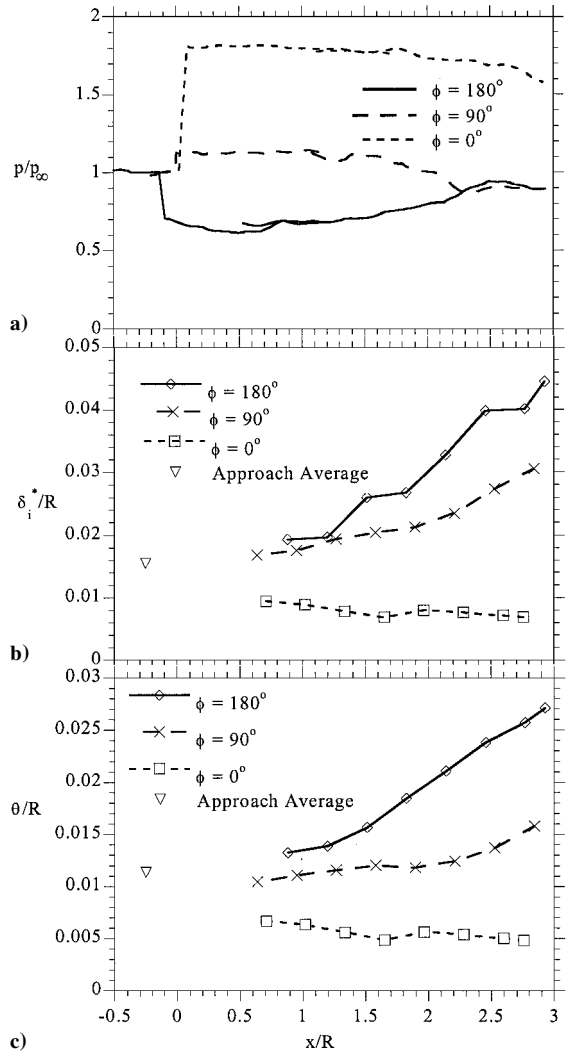

Fig. 8 Axial variation of a) surface pressure, b) displacement thickness, and c) momentum thickness in all three planes.

the leeward region near the base edge. Because of this excess mass in the leeward region, additional mass that previously passed circumferentially through the boundary layer into the leeward region is prevented from reaching the leeward plane and begins to accumulate in the side region, thus resulting in an increase in displacement thickness near the base edge.

In the leeward region, δ_i^* grows in thickness to approximately 2.86 times larger than the approach displacement thickness. The increase in displacement thickness occurs as a result of the same three factors that facilitate boundary-layer thinning in the windward plane. First, the global decrease in surface pressure across the expansion fan provides a low-pressure region for boundary-layer growth. Second, an adverse pressure gradient develops on the downstream half of the afterbody (Fig. 8a), enhancing boundary-layer growth. Third, the windward-to-leeward surface flow results in a mass surplus in the leeward plane, further facilitating boundary growth in the leeward region.

The boundary-layer velocity profiles were also integrated to compute the incompressible momentum thickness θ_i:

$$\theta_i = \int_R^\infty \frac{V_x}{V_{x,\infty}}\left(1 - \frac{V_x}{V_{x,\infty}}\right) \mathrm{d}r \qquad (2)$$

The axial variations in momentum thickness along the $\phi = 0, 90$, and 180 deg planes are plotted in Fig. 8c. The axial variations in momentum thickness closely follow the qualitative trends noted earlier for the displacement thickness. The changes in momentum thickness are also driven by similar mechanisms that control the variations in displacement thickness. Momentum efflux from the windward region and a favorable pressure gradient downstream of the compression shock result in a decrease of the momentum thickness in the windward plane. Similarly, the windward-to-leeward momentum flux created by the circumferential flow in the boundary layer and an adverse pressure gradient result in an axial increase in the leeward-plane momentum thickness. The momentum thickness on the $\phi = 90$ deg side plane remains relatively constant except in the most downstream region, where it increases modestly.

Turbulence Measurements

Plots of the axial normal stress, nondimensionalized by the square of the freestream approach velocity, $\langle v_x'^2\rangle / V_\infty^2$, in the boundary layer for all three measurement planes are included in Fig. 9. For Figs. 9a–9c, the location of highest measured stress is denoted with a star. In each of the measurement planes shown in Fig. 9, the axial stress in the boundary layer increases while approaching the afterbody surface. Note that the axial Reynolds stress is of generally comparable magnitude in all three measurement planes. Stress levels peak very near the wall, but the axial location of the maximum measured stress varies between the three measurement planes. The highest measured axial stress in the windward plane (Fig. 9a) is observed at $x/R \approx 0.4$, where $\langle v_x'^2\rangle / V_\infty^2 = 0.00521$. In the side plane (Fig. 9b), the location of maximum measured axial stress ($\langle v_x'^2\rangle / V_\infty^2 = 0.00666$) is observed slightly farther upstream, at $x/R \approx 0.35$, than in the windward plane. In the leeward plane (Fig. 9c), a small initial axial normal stress peak ($\langle v_x'^2\rangle / V_\infty^2 = 0.00282$) is found at $x/R \approx 0.1$, where the expansion fan interacts directly with the boundary layer. This initial peak is followed first by a slight decrease in normal stress and then an increase in stress to the maximum measured value of $\langle v_x'^2\rangle / V_\infty^2 = 0.00545$ near the surface at $x/R \approx 0.95$. Note that, in all

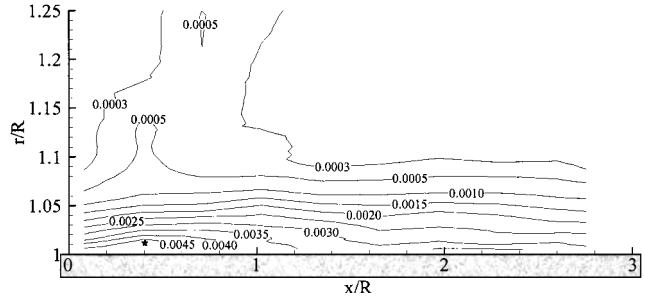

a) Windward plane, $\phi = 0$ deg

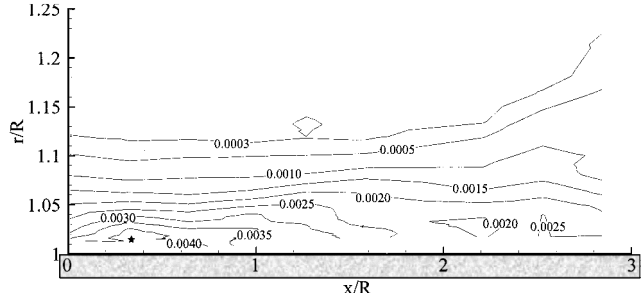

b) Side plane, $\phi = 90$ deg

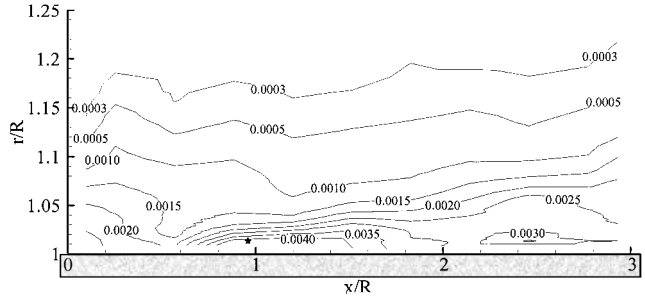

c) Leeward plane, $\phi = 180$ deg

Fig. 9 Axial normal stress contours $\langle v_x'^2\rangle / V_\infty^2$ in boundary layer.

three planes, the maximum axial stress is measured very near the inner limit of measurements completed in this investigation. Higher stress values may occur closer to the wall, where the presence of the surface clips the LDV beams, preventing velocity measurements.

As already discussed, the location of the maximum measured axial normal stress varies axially between the three circumferential planes. The location of this maximum measured stress region occurs slightly downstream of the shock in the windward region, then appears to move farther downstream as it passes into the leeward plane. This could be a result of the circumferential boundary-layer flow, which advects the high axial stress fluid behind the oblique shock from the windward region into the side and leeward planes. This can be seen most clearly in the leeward plane, where the increase in axial stress from the expansion fan is initially dissipated, but the axial stress then increases from the influx of high axial stress fluid from the windward region. Note that there is also an apparent increase of axial stress observed in the windward plane in the region of the oblique shock outside the boundary layer. This apparent stress increase is most likely a false turbulence caused by slight unsteadiness of the shock position. This nonphysical turbulence near the oblique shock may also be caused by the variation of silicone oil droplet sizes used to seed the flow. Because larger droplets decelerate at a slower rate than smaller droplets, this differing deceleration rate between individual seed droplets can create nonphysical variations in the measurement of instantaneous fluid velocity.

These axial normal stresses measured about the cylindrical body are similar qualitatively to the axial velocity fluctuations measured by Ausherman and Yanta[14] on cones at angle of attack. Both sets of data show axial velocity fluctuations peaking near the wall, with the peaks of similar magnitude in all circumferential planes. However, the conical data provide no evidence of circumferential variation of the axial location of the peak axial normal stress. Instead, the peak axial velocity fluctuations remained of relatively constant magnitude throughout their axial development along the cone.

The amplification of axial normal stress across the angular discontinuity is most evident through observation of individual normal stress profiles as shown in Figs. 10 and 11 for the windward and leeward planes, respectively. In the windward plane, the axial normal stress in the boundary layer decreases slightly across the oblique shock, then increases to a postshock peak level near $x/R = 0.4$. Note, however, that this peak level downstream of the shock is of approximately equal magnitude to the peak axial normal stress measured upstream of the shock. This result is in contrast to the data of Kuntz et al.,[23] who found a significant increase in streamwise turbulence fluctuations across a two-dimensional compression corner. In addition, Kuntz et al. noted the location of the peak fluctuations in the boundary layer moving away from the wall to near the center of the boundary layer with increasing x. The current data suggest that the peak axial stress remains very close to the wall, at a distance nearing the inner spatial limit where the data could be obtained.

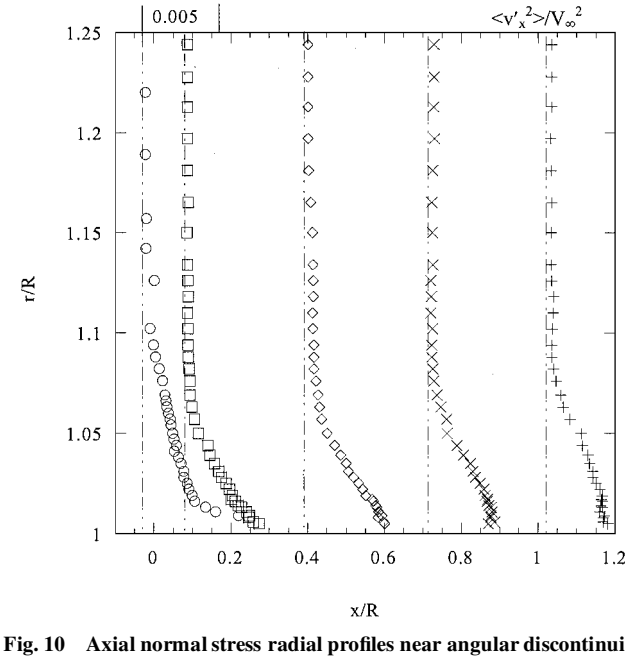

Fig. 10 Axial normal stress radial profiles near angular discontinuity in windward plane.

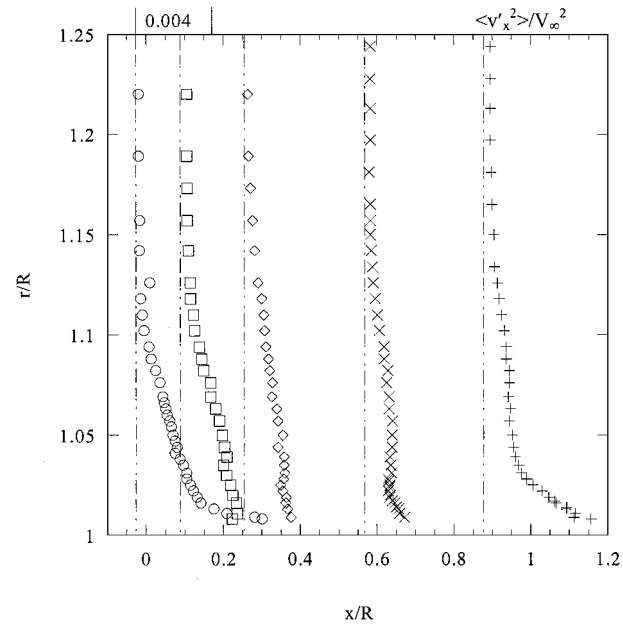

Fig. 11 Axial normal stress radial profiles near angular discontinuity in leeward plane.

In the leeward plane (Fig. 11), the axial normal stress first decreases near the wall compared to the approach axial normal stress magnitude, then begins to recover toward the approach profile. The presence of the expansion fan near the leeward surface appears to initially stabilize the axial velocity fluctuations in the boundary layer. This decrease in axial stress across the expansion from the approach levels agrees with the results of Arnette et al.[24] for a 7-deg planar centered expansion. However, the results of Arnette et al. do not suggest a recovery of the axial stress magnitude toward the approach levels, but instead the stress profiles approach a similar shape, with magnitude lower than the approach axial normal stress. The increase in axial stress magnitude downstream in the current data is most likely caused by the growth of the boundary layer, which provides lower speed fluid with higher axial velocity fluctuations at the same distance from the wall for increasing x.

Contour plots of the nondimensional radial normal stress, $\langle v_r'^2 \rangle / V_\infty^2$, through the boundary layer in all three planes, are included in Fig. 12. (Again, the location of highest measured stress is denoted by a star.) Note that, although the stresses increase in the inner portion of the boundary layer, the measured maximum radial stress magnitude varies fairly substantially from plane to plane, in contrast to the behavior of the axial stress. This can be most easily observed by noting the contour levels in Figs. 12a–12c. The radial stress magnitude on the windward side of the afterbody is approximately twice as large as that observed in the leeside boundary layer. This increase in radial stress magnitude is most likely due to a radial stress amplification mechanism that occurs in the shock/boundary-layer interaction at the compression turn. This radial stress amplification does not appear to occur as strongly as a result of the expansion turn on the leeward plane.

The radial stress once again tends to peak in the inner region of the boundary layer, but the axial location of the radial stress peak varies much more than that observed in the axial stress contours. The highest measured radial stress in the windward plane is observed just downstream of the oblique shock, at $x/R \approx 0.4$, where $\langle v_r'^2 \rangle / V_\infty^2 = 0.00561$. This windward radial stress maximum is much larger than that measured in the other planes and is of approximately equal magnitude to the highest measured axial normal stress in this plane. In the side plane, the location of the maximum measured radial normal stress ($\langle v_r'^2 \rangle / V_\infty^2 = 0.00313$) is observed at the location

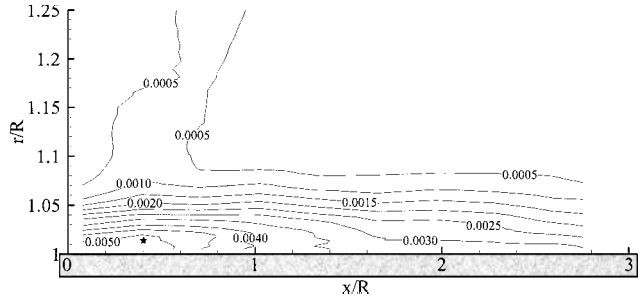

a) Windward plane, $\phi = 0$ deg

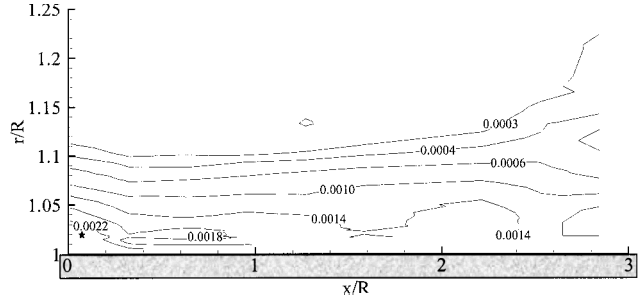

b) Side plane, $\phi = 90$ deg

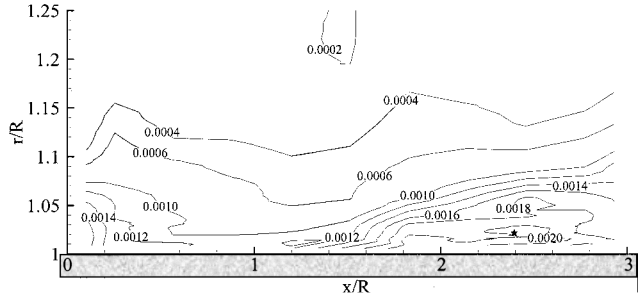

c) Leeward plane, $\phi = 180$ deg

Fig. 12 Radial normal stress contours $\langle v_r'^2 \rangle / V_\infty^2$ in boundary layer.

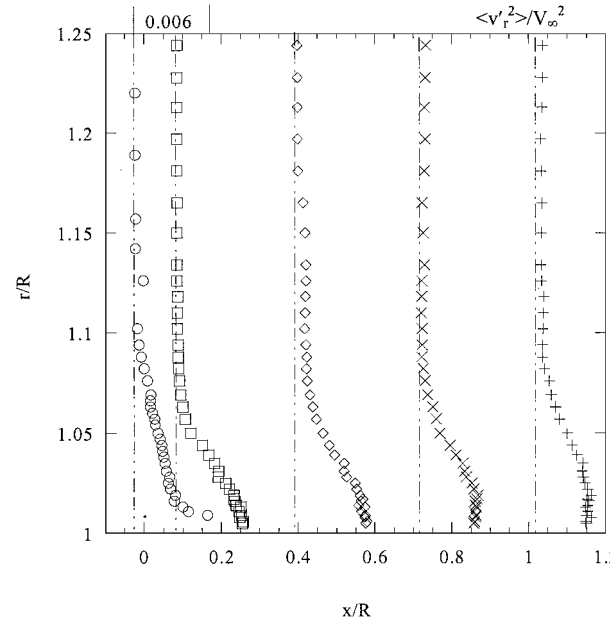

Fig. 13 Radial normal stress radial profiles near angular discontinuity in windward plane.

of the angular discontinuity, $x/R \approx 0.05$, and a smaller magnitude secondary stress peak is observed farther downstream, at $x/R \approx 2.2$. The radial stress in the leeward portion of the boundary layer initially peaks ($\langle v_r'^2 \rangle / V_\infty^2 = 0.00182$) just downstream of the angular discontinuity, $x/R \approx 0.1$, due to the interaction of the expansion fan with the boundary layer. This initial radial stress peak dissipates axially, but then increases to the maximum measured value of $\langle v_r'^2 \rangle / V_\infty^2 = 0.00226$ at $x/R \approx 2.4$. This region of high radial stress is elliptical in shape and is much larger in size than that observed in the axial stress contours. In addition, this region of high radial stress in the leeward region is much farther downstream than that observed for the axial stress. The presence of this radial stress peak near the base edge may suggest incipient separation in this downstream region. This maximum measured radial stress is less than half as large in magnitude as that measured for the axial stress in the leeward plane. There is no clear evidence of transport of high radial stress fluid from the windward plane, through the side plane, and into the leeward region by means of the circumferential boundary-layer flow, as was observed in the axial stress results. Once again, there is also a slight increase of radial stress observed in the windward plane outside the boundary layer in the region of the oblique shock, similar to that observed in the axial stress contours, as a result of shock unsteadiness and/or the polydispersed size distribution of the seed particles.

These radial normal stress results differ significantly from the radial velocity fluctuation data previously published for supersonic cones at angle of attack.[14] In the conical data, radial velocity fluctuations remained fairly constant across the boundary layer, unlike the distinct peak noted in the current cylindrical data in the inner portion of the boundary layer, especially in the high-magnitude windward plane. The lack of a peak in the cone data may occur because measurements were reported only in the outer 80% of the boundary layer, allowing for a peak to potentially occur in the inner 20%, where no measurements were obtained. In addition, the radial fluctuation magnitude in the conical data does not vary with circumferential location, unlike the current data for which a significantly higher radial normal stress is observed in the windward plane. This difference in radial stress amplification in the windward plane most likely results because the boundary layer on the cone initiates at its tip, just downstream of the leading oblique shock. Because the boundary layer has no significant thickness at the cone tip, there is no boundary layer present for which the shock may amplify the radial velocity fluctuations.

Radial normal stress profiles are shown in Fig. 13 for the windward plane just downstream of the compression shock. Near the wall, the radial stress peak appears to decrease slightly across the oblique shock before decreasing further in magnitude with increasing x. In addition, the radial region of high radial stress in each profile appears to broaden slightly with increasing x just downstream of the shock. Unlike this slight decrease in radial normal stress across the oblique shock, Kuntz et al.[23] noted an increase in wall-normal stress across a planar compression shock, to levels approximately double the approach radial normal stress. In addition, Kuntz et al. noted a fairly flat radial stress profile with no significant radial variations. In contrast, the highest radial normal stress appears near the wall in the current data, with the high stress region broadening with increasing x.

In the leeward plane (Fig. 14), the radial normal stress is clearly strongly damped across the expansion fan and decreases further in magnitude with increasing x. This decrease in radial stress agrees with the findings of Arnette et al.[24] for a planar expansion. The profiles of radial stress for the current case are also significantly broader and flatter than the profiles in the windward region. In addition to viscous diffusion of high-stress fluid from the windward region, this broadening is most likely due to the increasing thickness of the leeward boundary layer with increasing x, which provides lower speed and higher radial stress fluid farther from the wall.

Contour plots of the dimensionless axial–radial Reynolds shear stress, $-\langle v_x' v_r' \rangle / V_\infty^2$, are included in Fig. 15. The Reynolds shear stress follows the same general trends observed in the normal stresses, with the stress generally increasing toward the surface across the boundary layer. (The location of highest measured stress is denoted with a star.) The shear stress is of approximately equal magnitude in each measurement plane. The highest measured Reynolds shear stress in the windward plane is observed at the interaction

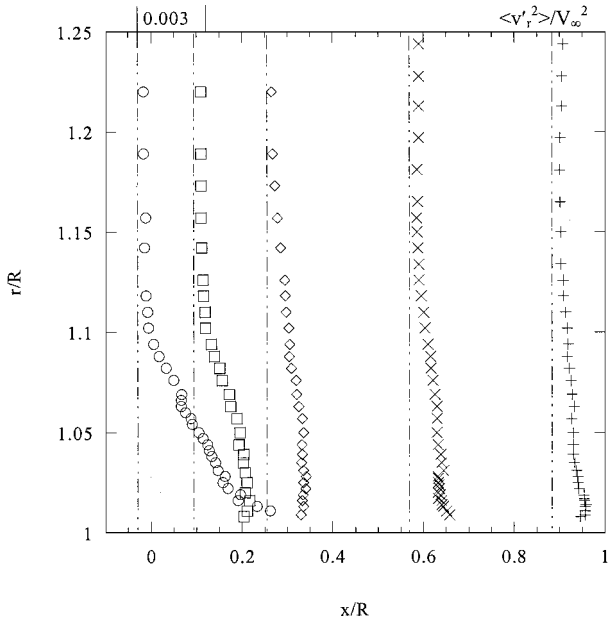

Fig. 14 Radial normal stress radial profiles near angular discontinuity in leeward plane.

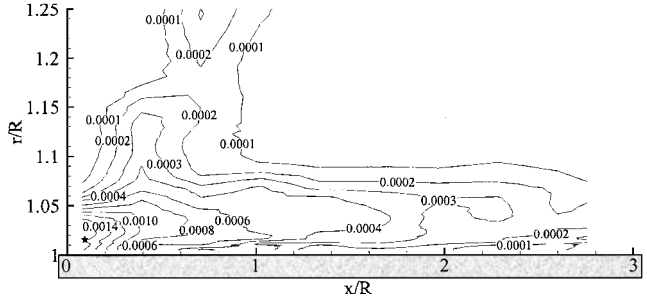

a) Windward plane, $\phi = 0$ deg

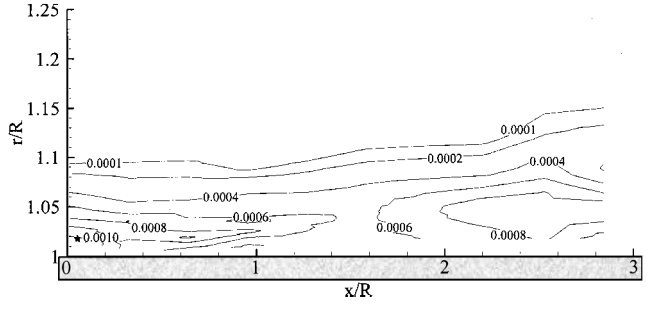

b) Side plane, $\phi = 90$ deg

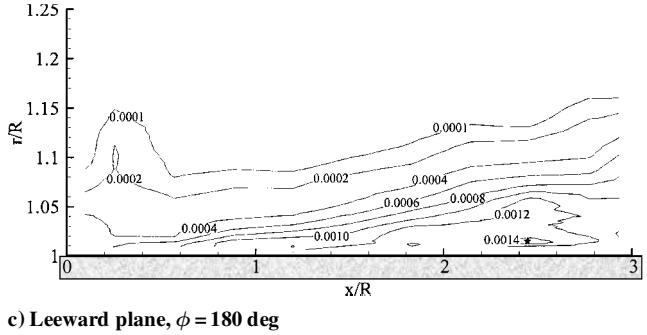

c) Leeward plane, $\phi = 180$ deg

Fig. 15 Axial–radial Reynolds shear stress contours $-\langle v'_x v'_r \rangle / V_\infty^2$ in boundary layer.

of the oblique shock with the boundary layer at $x/R \approx 0.05$, where $-\langle v'_x v'_r \rangle / V_\infty^2 = 0.00186$. In the side plane, the location of maximum measured Reynolds shear stress ($-\langle v'_x v'_r \rangle / V_\infty^2 = 0.00132$) is observed just downstream of the angular discontinuity, $x/R \approx 0.05$, with a secondary stress peak observed farther downstream at $x/R \approx 2.5$, where $-\langle v'_x v'_r \rangle / V_\infty^2 = 0.00119$. In the leeward portion of the boundary layer, the shear stress reaches a measured maximum of $-\langle v'_x v'_r \rangle / V_\infty^2 = 0.00168$ near the base edge, at $x/R \approx 2.5$. Overall, the shapes of these Reynolds shear stress contours and the location of the shear stress peaks more closely match the radial normal stress results than the axial normal stress results. However, the approximately equal magnitude of shear stress in each measurement plane agrees with the observation of nearly equal axial normal stress magnitudes in each measurement plane. The conical data of Ausherman and Yanta[14] display similar trends between the axial velocity fluctuations and the axial–radial shear stress. However, as was seen with the axial fluctuations, little axial variation in the axial–radial shear stress magnitude was observed in the conical data.

Axial–radial Reynolds shear stress profiles just downstream of the angular discontinuity are shown in Figs. 16 and 17 for the windward and leeward planes, respectively. In the windward plane, the compression shock is seen initially to reduce the peak shear stress magnitude and broaden the region of peak shear stress. Moving farther downstream, the shear stress dissipates to levels lower than that just downstream of the shock. The radial region of peak stress continues to broaden with increasing axial displacement as well. The initial decrease in peak shear stress contrasts with the two-dimensional compression corner result of Kuntz et al.[23] The two-dimensional results note a significant increase in shear stress across the compression shock, followed by a damping to lower stress during the downstream development of the boundary layer. However, even the reduced shear stress magnitudes far downstream from the compression shock in the two-dimensional results remain significantly higher than the shear stress observed in the approach flow. The decrease in shear stress just downstream of the shock observed for the current case may be a result of the circumferential flow along the afterbody, which provides an efflux of high-stress fluid out of the windward region.

In the leeward region (Fig. 17), the expansion fan appears to reduce significantly the peak axial–radial shear stress in the boundary layer from the approach magnitudes. Downstream of the expansion fan, the shear stress levels begin to increase in magnitude, but do not reach the levels measured in the approach boundary layer. This result agrees favorably with the study of Arnette et al.[24] for a 7-deg

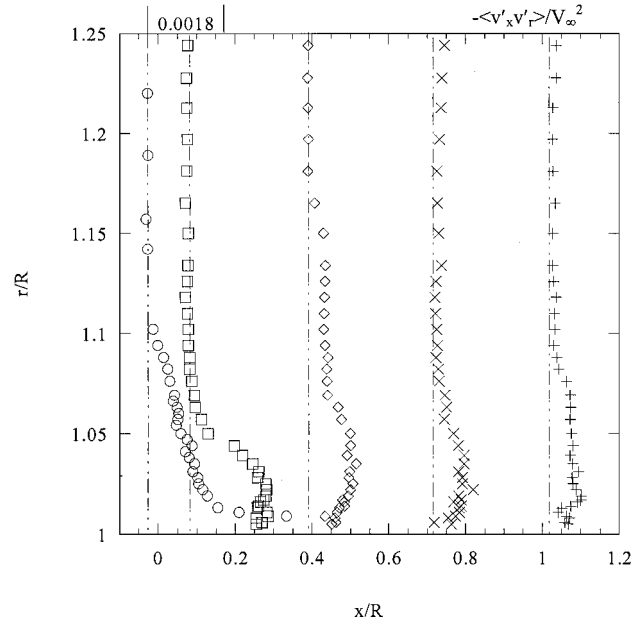

Fig. 16 Axial–radial Reynolds shear stress radial profiles near angular discontinuity in windward plane.

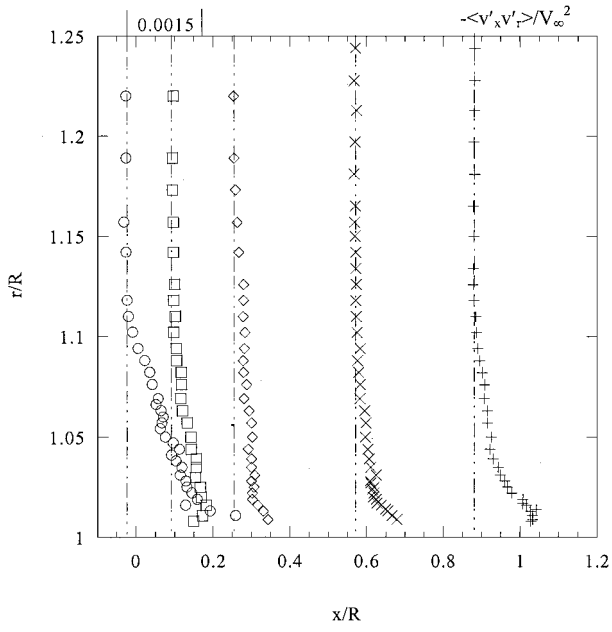

Fig. 17 Axial–radial Reynolds shear stress radial profiles near angular discontinuity in leeward plane.

two-dimensional centered expansion. Unlike the windward region, the peaks in shear stress for the current measurements appear to be confined very near the afterbody surface in the leeward plane.

Conclusions

LDV has been used to measure the mean velocity and turbulence fields in a three-dimensional, pressure-driven, turbulent, compressible boundary layer. The boundary layer was generated by inclining a cylindrical afterbody to 10-deg angle of attack in a Mach 2.45 freestream. This study permits determination of the physical behavior of this three-dimensional boundary layer and provides understanding of the fluid dynamic processes that occur on cylindrical afterbodies when inclined at nonzero angle of attack. Based on the velocity measurements, the following conclusions may be drawn:

1) The angular discontinuity used to create the 10-deg angle of attack results in a complex compression wave/expansion fan of circumferentially varying strength. In the windward plane, the discontinuity appeared approximately as an oblique shock generated at a 10-deg planar compression corner in Mach 2.45 flow. On the side, $\phi = 90$ deg, plane, a small flow deceleration occurred at a position approximately equivalent to a Mach wave in $M = 2.45$ flow. Previously measured pressure data (Fig. 8a) suggest a weak compression in this plane. The small deflection of representative streamlines in this plane confirms that the discontinuity on this side plane is a weak compression. In the leeward plane, the discontinuity occurred at a position approximately equivalent to a Prandtl–Meyer expansion fan for a 10-deg planar expansion corner in a Mach 2.45 freestream.

2) The boundary layer is seen to compress on the windward side of the body, grow slightly along the axial extent of the side plane, and grow rapidly on the leeward side of the body throughout its entire axial development. The change in thickness of the three-dimensional boundary layer appears to be controlled by three factors. First, the angular junction creates a pressure discontinuity of circumferentially varying strength. This pressure change should compress the windward portion of the boundary layer and expand the leeside boundary layer. Second, a circumferential flow in the boundary layer provides a transfer of mass and low-momentum fluid into the growing leeward boundary layer from the shrinking windward boundary layer. Third, the axial pressure gradient about the afterbody tends to increase the boundary-layer thickness in regions of adverse pressure gradients and to retard the boundary-layer growth in regions of favorable pressure gradients. Thus, the balance between these three factors governs the overall increase or decrease in thickness throughout the axial development of this three-dimensional, pressure-driven boundary layer.

3) The regions of significant Reynolds normal and shear stresses are confined to the boundary layer, with peaks in turbulent stresses found near the wall. All turbulent stresses are reduced in magnitude in passage across the angular discontinuity. Axial normal stresses tend to be greater in magnitude than the radial normal stresses. Peaks in axial normal stress tend to occur farther upstream on the windward side of the afterbody, which suggests that turbulence generated in the oblique shock/boundary-layer interaction was advected to the leeward side of the afterbody by the circumferential flow in the boundary layer. The magnitude of radial normal stress in the windward plane is higher than in either the leeward or side planes, which suggests that the interaction between the leading oblique shock and boundary layer amplifies radial velocity fluctuations. Although no flow separation has been observed or measured in the leeward region,[15] the presence of a peak in radial normal stress that forms near the base edge in the leeward plane may indicate incipient separation in this plane.

Acknowledgments

This work was supported by the U.S. Army Research Office, under Grant DAAG-55-97-1-0122 with Thomas L. Doligalski as Technical Monitor.

References

[1]Oberkampf, W. L., and Bartel, T. J., "Symmetric Body Vortex Wake Characteristics in Supersonic Flow," *AIAA Journal*, Vol. 18, No. 11, 1980, pp. 1289–1297.

[2]Johnston, J. P., and Flack, K. A., "Review-Advances in Three-Dimensional Turbulent Boundary Layers with Emphasis on the Wall-Layer Regions," *Journal of Fluids Engineering,* Vol. 118, No. 2, 1996, pp. 219–232.

[3]Chesnakas, C. J., and Simpson, R. L., "Full Three-Dimensional Measurements of the Cross-Flow Separation Region of a 6:1 Prolate Spheroid," *Experiments in Fluids,* Vol. 17, No. 1/2, 1994, pp. 68–74.

[4]Knight, D. D., Horstman, C. C., Shapey, B., and Bogdonoff, S., "Structure of Supersonic Turbulent Flow Past a Sharp Fin," *AIAA Journal,* Vol. 25, No. 10, 1987, pp. 1331–1337.

[5]Demetriades, A., and McCullough, G., "Mean-Flow Measurements in a Supersonic Three-Dimensional Turbulent Boundary Layer," *Journal of Fluid Mechanics,* Vol. 156, 1985, pp. 401–418.

[6]Knight, D. D., Horstman, C. C., and Bogdonoff, S., "Structure of Supersonic Turbulent Flow Past a Swept Compression Corner," *AIAA Journal,* Vol. 30, No. 4, 1992, pp. 890–896.

[7]Konrad, W., Smits, A. J., and Knight, D., "A Combined Experimental and Numerical Study of a Three-Dimensional Supersonic Turbulent Boundary Layer," *Experimental Thermal and Fluid Science,* Vol. 9, No. 2, 1994, pp. 156–164.

[8]Konrad, W., and Smits, A. J., "Turbulence Measurements in a Three-Dimensional Boundary Layer in Supersonic Flow," *Journal of Fluid Mechanics,* Vol. 372, 1998, pp. 1–23.

[9]Konrad, W., Smits, A. J., and Knight, D., "Mean Flowfield Scaling of Supersonic Shock-Free Three-Dimensional Turbulent Boundary Layer," *AIAA Journal,* Vol. 38, No. 11, 2000, pp. 2120–2126.

[10]Brown, J. D., Brown, J. L., and Kussoy, M. I., "A Documentation of Two- and Three-Dimensional Shock-Separated Turbulent Boundary Layers," NASA TM 101008, 1988.

[11]Yanta, W. J., Ausherman, D. W., and Hedlund, E., "Measurements of a Three-Dimensional Boundary Layer on a Sharp Cone at Mach 3," AIAA Paper 82-0289, 1982.

[12]Yanta, W. J., and Ausherman, D. W., "The Turbulence Transport Properties of a Supersonic Boundary Layer on a Sharp Cone at Angle of Attack," AIAA Paper 83-0456, 1983.

[13]Ausherman, D. W., Yanta, W. J., and Rutledge, W. H., "Measurement of the Three-Dimensional Boundary Layers on Conical Bodies at Mach 3 and Mach 5," AIAA Paper 83-1675, 1983.

[14]Ausherman, D. W., and Yanta, W. J., "The Three-Dimensional Turbulence Transport Properties in the Boundary Layers of Conical Body Configurations at Mach 3," AIAA Paper 84-1528, 1984.

[15]Boswell, B. A., and Dutton, J. C., "Flow Visualizations and Measurements of a Three-Dimensional Supersonic Separated Flow," *AIAA Journal,* Vol. 39, No. 1, 2001, pp. 113–121.

[16]Herrin, J. L., and Dutton, J. C., "Supersonic Base Flow Experiments in the Near Wake of a Cylindrical Afterbody," *AIAA Journal,* Vol. 32, No. 1, 1994, pp. 77–83.

[17]Mathur, T., and Dutton, J. C., "Velocity and Turbulence Measurements in a Supersonic Base Flow with Mass Bleed," *AIAA Journal,* Vol. 34, No. 6, 1996, pp. 1153–1159.

[18]Bloomberg, J. E., "An Investigation of Particle Dynamics Effects Related to LDV Measurements in Compressible Flows," M.S. Thesis, Dept. of Mechanical and Industrial Engineering, Univ. of Illinois, Urbana, IL, May 1989.

[19]Herrin, J. L., and Dutton, J. C., "An Investigation of LDV Velocity Bias Correction Techniques for High Speed Separated Flows," *Experiments in Fluids,* Vol. 14, No. 4/5, 1993, pp. 354–363.

[20]Herrin, J. L., "An Experimental Investigation of Supersonic Axisymmetric Base Flows Including the Effects of Afterbody Boattailing," Ph.D. Dissertation, Dept. of Mechanical and Industrial Engineering, Univ. of Illinois, Urbana, IL, July 1993.

[21]Sun, C. C., and Childs, M. E., "A Modified Wall Wake Velocity Profile for Turbulent Compressible Boundary Layers," *Journal of Aircraft*, Vol. 10, No. 6, 1973, pp. 381–383.

[22]Mathur, T., and Dutton, J. C., "Base-Bleed Experiments with a Cylindrical Afterbody in Supersonic Flow," *Journal of Spacecraft and Rockets,* Vol. 33, No. 1, 1996, pp. 30–37.

[23]Kuntz, D. W., Amatucci, V. A., and Addy, A. L., "Turbulent Boundary-Layer Properties Downstream of the Shock-Wave/Boundary-Layer Interaction," *AIAA Journal,* Vol. 25, No. 5, 1987, pp. 668–675.

[24]Arnette, S. A., Samimy, M., and Elliott, G. S., "The Effects of Expansion on the Turbulence Structure of Compressible Boundary Layers," *Journal of Fluid Mechanics,* Vol. 367, 1998, pp. 67–105.

J. P. Gore
Associate Editor